



Universiteit
Leiden
The Netherlands

Accurate modeling of the dynamics of dissociative chemisorption on metal surfaces

Gerrits, N.

Citation

Gerrits, N. (2021, September 23). *Accurate modeling of the dynamics of dissociative chemisorption on metal surfaces*. Retrieved from <https://hdl.handle.net/1887/3213516>

Version: Publisher's Version

License: [Licence agreement concerning inclusion of doctoral thesis in the Institutional Repository of the University of Leiden](#)

Downloaded from: <https://hdl.handle.net/1887/3213516>

Note: To cite this publication please use the final published version (if applicable).

Chapter 6

The Curious Reaction Mechanism of Ammonia on Ru(0001)

This chapter is based on Gerrits, N.; Kroes, G.-J. Curious Mechanism of the Dissociative Chemisorption of Ammonia on Ru(0001). *J. Phys. Chem. C* **2019**, *123*, 28291–28300, DOI: [10.1021/acs.jpcc.9b09121](https://doi.org/10.1021/acs.jpcc.9b09121)

Abstract

Dissociative chemisorption of polyatomic molecules on metals, which is relevant to heterogeneous catalysis, usually proceeds through a rotationally adiabatic or rotational sudden mechanism. The reaction is usually either direct, or proceeds through a trapped molecular physisorped state. Here, *ab initio* molecular dynamics is used to model the dissociative chemisorption of ammonia on Ru(0001). The reaction mechanism is neither rotationally adiabatic nor rotational sudden, with clearly distinct and non-statistical initial and time-of-reaction orientation distributions. Reasonably good agreement is obtained between computed and previously measured sticking probabilities. Under the conditions investigated the reaction of NH₃ goes through a molecular chemisorption-like state, but the reaction is direct.

6.1 Introduction

Recent ab initio molecular dynamics (AIMD)[1–7] and quasi-classical trajectory (QCT)[8, 9] calculations on high-dimensional potential energy surfaces (PESs) are providing a wealth of information on the dynamics of polyatomic molecules reacting on metal surfaces. Of these, direct reactions on metal surfaces are typically either rotationally adiabatic[10] (e.g., water + Ni(111)[4, 11]) or in a sudden regime[12, 13] (e.g., CHD₃ + Pt(111)[5] and methanol + Cu(111)[7] (see also Chapter 10)). In the former case, the initial orientation distribution of the reacting molecules is statistical (i.e., it resembles a $\sin(\theta)$ distribution of the θ_d angle shown in Figure 6.1a) and is steered towards transition state (TS) values[4]. In the latter case, the initial orientation distribution is already close to the orientation at the barrier geometry[5, 7, 14, 15]. Approximate methods such as the Reaction Path Hamiltonian (RPH) approach[16] often use either a rotationally adiabatic or a sudden approximation[13, 14]. Furthermore, if a reaction proceeds through a molecular chemisorption-like state, it is usually trapping mediated[3]. However, as will be shown here, ammonia reacts on Ru(0001) through a very different mechanism, in which both the incident orientation distribution and the distribution at the TS are non-statistical, but clearly distinct. Furthermore, the reaction is observed to be direct, even though the molecule proceeds through a molecular chemisorption-like geometry as observed in trapping-mediated reaction.

Due to the high pressures and temperatures involved in the Haber-Bosch process[18], whereby N₂ is converted to NH₃, ammonia is not only a product in this process, but also a reactant, and Ru is a good catalyst for ammonia production[19]. Therefore, predicting and understanding the reaction of ammonia on Ru(0001) is not only of interest for fundamental reasons, it is also of practical importance, as NH₃ is a raw material for the production of synthetic fertilizer that helps feed a substantial part of the world's population[20]. Additionally, Ru is the best single metal catalyst for ammonia decomposition[21–23], which is relevant to the production of CO_x-free H₂ for hydrogen fuel cell applications[22]. In the kinetics of ammonia decomposition, the breaking of the first NH-bond is an important step[22–24].

Molecular beam sticking experiments on dissociative chemisorption of ammonia on Ru(0001) have been performed by Mortensen et al.[25] at surface temperatures (T_s) of 475 and 1100 K. They found the dissociation to be activated and independent of T_s at incidence energies larger than 85 kJ/mol. Consequently, they proposed a direct reaction mechanism for these conditions. For the lower E_i their detailed experiments allowed them to propose a mechanism involving a molecularly chemisorbed state reacting at defect sites. In the

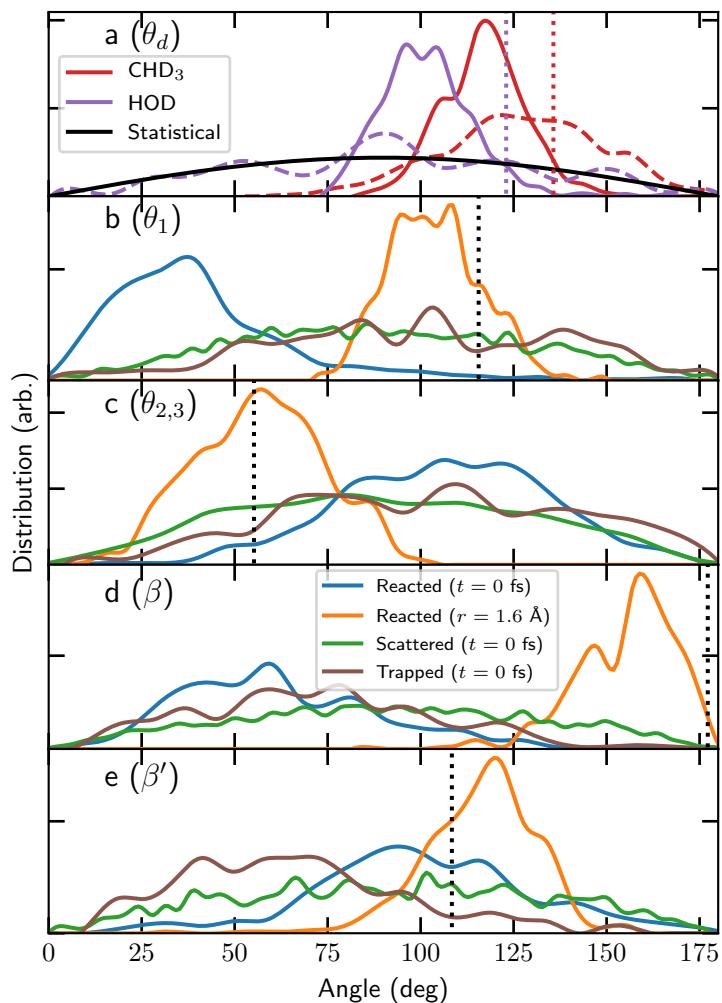


FIGURE 6.1: (a) θ_d angle (i.e., the dissociating bond) of CHD_3 [17] (red) and HOD [4] (purple) for all reacted trajectories at the initial time step (dashed lines) and when a dissociating bond reaches the TS value (solid lines). The solid black line indicates a statistical $\sin(\theta)$ distribution. The dotted lines indicate the TS values. (b, c, d, e) θ_1 , $\theta_{2,3}$, β , and β' angles of ammonia for all scattered (green), trapped (brown), and reacted trajectories, where the results for the reacted trajectories are shown at the initial time step (blue) and when the dissociating bond reaches the TS value (orange). The angles of the non-dissociating hydrogen atoms with respect to the surface normal are indicated by $\theta_{2,3}$. β' indicates the angle between the surface normal and the umbrella axis, which is defined as the vector going from the geometric center of the three hydrogen atoms to the nitrogen atom. The dotted lines indicate the TS values belonging to the top2fcc barrier geometry.

latter mechanism, diffusion of reactants to and products away from the defects limits the sticking at very low T_s , and desorption of NH_3 prior to reaching the defects limits trapping-mediated reaction at high T_s .

So far, only Hu et al.[26] used dynamics calculations to model the experimentally measured sticking probabilities on $\text{NH}_3 + \text{Ru}(0001)$, performing QCT calculations on a twelve-dimensional (12D) PES fitted with a neural network approach[27]. Their work focused on vibrational enhancement of the reaction, and they found vibrational efficacies near unity for each of the four vibrational modes of NH_3 . Although the dynamical behaviour of the ammonia molecule was included, the metal surface atoms were kept frozen. They did not model energy transfer to the surface atoms, even though this can play a major role in the computed reactivity for molecule-metal surface reactions[8, 12, 13]. The Perdew, Burke and Ernzerhof (PBE) exchange-correlation (xc) density functional (DF)[28] was used. For high incidence energies the computed sticking probabilities for NH_3 in its initial vibrational ground state were considerably higher (by a factor 2 - 2.5) than the experimental sticking probabilities, which the authors attributed to the use of the PBE DF. Indeed, this DF, like its very similar[28] predecessor PW91[29], often overestimates the reactivity of molecules on metal surfaces[5, 30–33] (see also Chapter 5 where the ease of charge transfer between the molecule and metal surface is related to the ability of a DF to accurately describe a molecule-metal surface barrier height).

Here, the reaction is studied at the higher incidence energy conditions for which the experimentalists did not yet characterize the reaction mechanism in detail, and for which AIMD calculations can be used: For high incidence energies the system can be kept small as defects do not play an important role, and propagation times can be kept short. In the AIMD calculations, the motions of NH_3 as well as that of the surface atoms of Ru(0001) are modelled explicitly. Different aspects are addressed of the reaction mechanism, i.e., the orientation distribution of the reacting molecules, and the role of the molecular chemisorption state in the reaction at high incidence energies. A DF is used containing revised PBE (RPBE)[34] exchange (more repulsive than PBE exchange) and the Van der Waals correlation DF of Dion et al. (vdW-DF1)[35], and is therefore called the RPBE-vdW-DF1 DF. In this chapter, it is shown that the reaction proceeds through an unusual mechanism, in which the initial orientation distribution of the reacting molecules is non-statistical, but is clearly distinct from the non-statistical distribution at the time of reaction, which resembles the orientation at the TS. Additionally, although the reaction is direct, the reacting molecules go through a geometry that is similar to the geometry that would be taken on by the molecular

precursor state dominating the reaction mechanism at low E_i . Compared to the earlier dynamics calculations[26] the agreement with the experimental sticking probabilities is improved.

6.2 Method

For the AIMD and electronic structure (Density Functional Theory, DFT) calculations the Vienna Ab-initio Simulation Package (VASP version 5.3.5)[36–40] is used. The first Brillouin zone is sampled by a Γ -centered $4 \times 4 \times 1$ k -point grid and the plane wave basis set kinetic energy cutoff is 400 eV. Moreover, the core electrons have been represented with the projector augmented wave (PAW) method[40, 41]. The surface is modeled using a 4 layer (3×3) supercell, where the top three layers have been relaxed in the Z direction and a vacuum distance of 15 Å is used between the slabs. Due to the use of the vdW-DF1 correlation DF the employed vacuum distance causes a small interaction energy between the surface and the molecule in the gas phase, which effectively raises the barrier height by 3.0 kJ/mol. However, due to the computational cost a larger vacuum distance is untractable in the AIMD. Therefore, 3.0 kJ/mol is added to the translational energy to counteract this shift (see Section 2.4.2). In order to speed up convergence, first-order Methfessel-Paxton smearing[42] with a width parameter of 0.2 eV has been applied. The employed computational setup is confirmed to be converged within chemical accuracy (1 kcal/mol, or 4.2 kJ/mol), as shown in Section 6.A.

Transition states are obtained with the dimer method[43–46] as implemented in the VASP Transition State Tools package (VTST)[47], and are confirmed to be first-order saddle points. Forces on the degrees of freedom are converged within 5 meV/Å, where only the ammonia is relaxed in all its degrees of freedom, i.e., when computing TSs the surface is kept fixed in its relaxed surface-vacuum geometry.

The RPBE-vdW-DF1 DF is used, which is defined as

$$E_{xc} = E_x^{\text{RPBE}} + E_c^{\text{vdW-DF1}}, \quad (6.1)$$

where E_x^{RPBE} is the exchange part of the revised Perdew, Burke and Ernzerhof (RPBE)[34] exchange-correlation DF and $E_c^{\text{vdW-DF1}}$ is the non-local Van der Waals correlation DF of Dion et al. (vdW-DF1)[35].

A surface temperature of 475 K and 1100 K is simulated in the AIMD calculations, where the atoms in the top three layers are allowed to move. The

TABLE 6.1: Thermal expansion coefficients for the a and c lattice vectors, which are taken from Ref. [48].

Temperature (K)	$\alpha_a(\text{K}^{-1})$	$\alpha_c(\text{K}^{-1})$
475	1.00110	1.00168
1100	1.00684	1.01045

TABLE 6.2: Experimental beam parameters that describe the simulated NH_3 velocity distributions. v_0 and α are based on time-of-flight measurements on CHD_3/H_2 beams (see the text)[17, 50].

T_n (K)	$\langle E_i \rangle$ (kJ/mol)	v_0 (m/s)	α (m/s)
400[50]	74.0	2899	290
500[50]	89.2	3157	316
600[17]	102.9	3418	342
700[17]	119.5	3683	368

expansion of the bulk due to the surface temperature is simulated by multiplying[49] the computed ideal lattice constants ($a = 2.7524 \text{ \AA}$, $c = 4.3334 \text{ \AA}$) with the thermal expansion coefficients[48] that are provided in Table 6.1.

Since ammonia has a similar mass as methane, the parameters used to simulate the molecular beam bundles (the stream velocity and width parameters, see Table 6.2) are taken from Refs. [17] and [50], which reported experiments performed for $\text{CHD}_3 + \text{Pt}(111)$ and $\text{Ni}(111)$. The width parameter α is taken as 10% of the stream velocity v_0 , which is somewhat larger than was obtained for CHD_3 [17, 50]. Note that this procedure was not employed in Ref. [26], where ammonia was in its vibrational ground state and the velocity distribution was not taken into account. For every AIMD data point at a surface temperature of 475 K and 1100 K, 1000 and 500 trajectories were run, respectively, using a time step of 0.4 fs. Other technical details of the AIMD calculations and the sampling of the initial conditions can be found in recent work[17, 32, 50] and in Chapter 2. Note that since NH_3 is an oblate symmetric top rotor, the rotational states have been described in the same manner as for CHD_3 [17, 50] (see Section 2.4.2), which is also a symmetric top rotor.

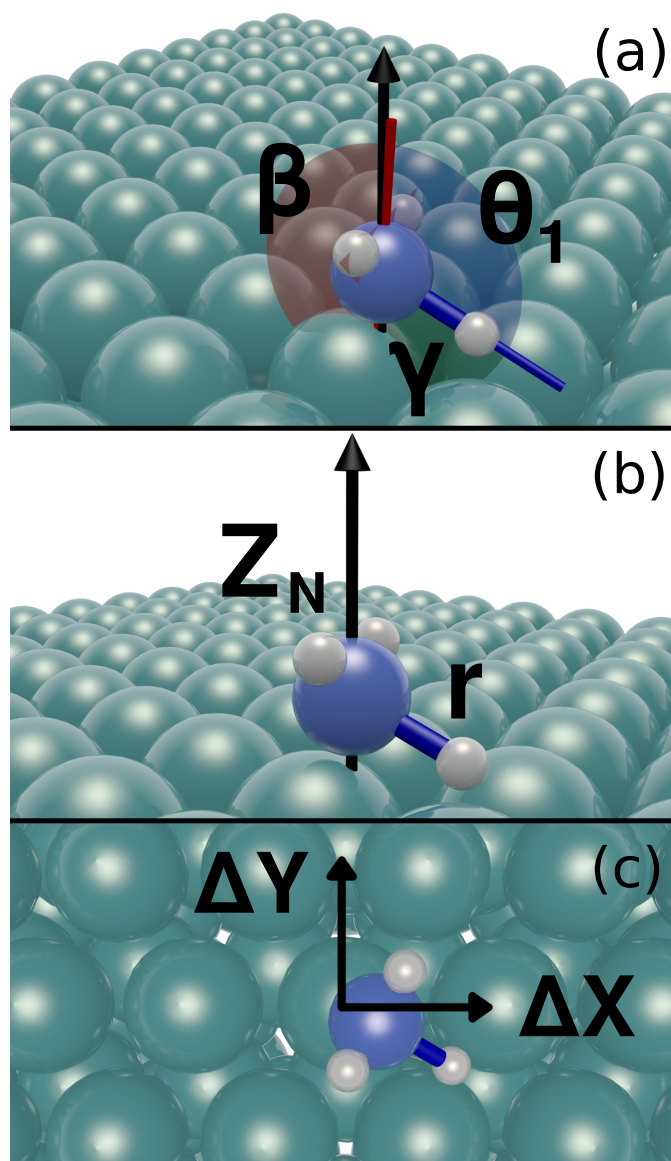


FIGURE 6.2: (a) Top2fcc TS of ammonia on Ru(0001), indicating the orientation angles as used in Table 6.3. θ_1 is the angle between the dissociating NH bond and the surface normal, β is the angle between the principal axis of NH_2 (i.e., the vector going from the geometric center of the two non-dissociating hydrogen atoms to the nitrogen atom) and the surface normal, and γ is the angle between θ_1 and this principal axis. (b) Same as panel a but here the length of the dissociating NH bond (r) and distance of the nitrogen atom to the surface (Z_N) are illustrated. (c) Top view of the top2fcc TS geometry.

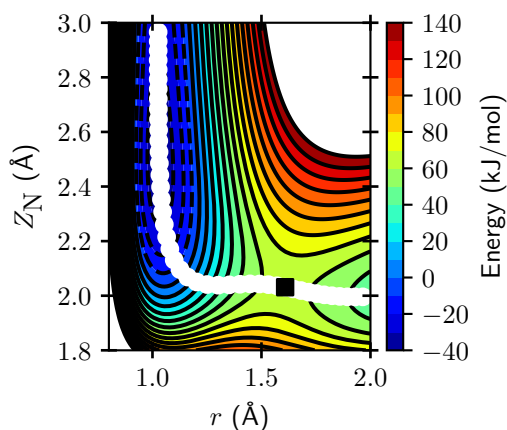
TABLE 6.3: Minimum barrier geometries and barrier heights of ammonia on Ru(0001) using different XC-DFs. The zero-point energy corrected barriers are given in the brackets. Barriers corrected for the usage of a too small vacuum distance are indicated by E_b^c .

Barrier	$Z_N(\text{\AA})$	$r(\text{\AA})$	$\theta_1(^{\circ})$	$\beta(^{\circ})$	$\gamma(^{\circ})$	E_b (kJ/mol)	E_b^c (kJ/mol)
top2fcc (RPBE-vdW)	2.04	1.62	115.6	177.2	61.6	65.9 (50.0)	62.9 (47.0)
top2hcp (RPBE-vdW)	2.03	1.60	116.1	176.5	60.3	63.2 (47.4)	60.2 (44.4)
top2fcc (SRP32-vdW)	2.01	1.62	113.8	177.6	63.9	41.4 (26.1)	38.4 (23.1)
top2hcp (SRP32-vdW)	2.01	1.59	114.8	175.0	60.2	42.0 (26.9)	39.0 (23.9)
top2fcc (PBE)	1.99	1.63	115.1	176.9	61.8	43.3 (29.6)	-
top2fcc (PBE)[26]	2.06	1.64	-	-	-	45.6 (31.8)	-
top2hcp (PBE)	1.99	1.61	115.6	176.2	60.6	40.2 (26.7)	-

TABLE 6.4: Top2fcc and top2hcp barrier geometries of ammonia on Ru(0001) using different XC-DFs. The relative cartesian coordinates of the nitrogen atom to the closest top atom are given by ΔX_N and ΔY_N and the distance between the nitrogen atom and the surface is given by Z_N . The positions of the hydrogen atoms relative to the nitrogen atom are given in spherical coordinates. The zero-point energy corrected barriers are given in the brackets and in kJ/mol. Barriers corrected for the usage of a too small vacuum distance are indicated by E_b^c .

	top2fcc (RPBE-vdW)	top2hcp (RPBE-vdW)	top2fcc (SRP32-vdW)	top2hcp (SRP32-vdW)	top2fcc (PBE)	top2hcp (PBE)
ΔX_N (Å)	0.47	0.00	0.51	0.00	0.45	0.00
ΔY_N (Å)	-0.28	-0.56	-0.29	-0.60	-0.25	-0.53
Z_N (Å)	2.04	2.03	2.01	2.01	1.99	1.99
r_{NH_1} (Å)	1.62	1.60	1.59	1.62	1.63	1.61
r_{NH_2} (Å)	1.02	1.02	1.02	1.02	1.02	1.02
r_{NH_3} (Å)	1.02	1.02	1.02	1.03	1.02	1.02
θ_{NH_1} (°)	115.6	116.1	114.8	113.8	115.1	115.6
θ_{NH_2} (°)	55.2	55.2	55.2	54.6	55.8	55.6
θ_{NH_3} (°)	55.3	55.2	55.4	55.9	55.5	55.7
ϕ_{NH_1} (°)	-30.0	-89.9	-29.7	-88.0	-30.1	-90.1
ϕ_{NH_2} (°)	61.9	2.5	63.3	0.7	62.2	2.6
ϕ_{NH_3} (°)	-122.0	177.6	-123.6	177.6	-122.0	177.4
E_b (kJ/mol)	65.9 (50.0)	63.2 (47.4)	41.4 (26.1)	42.0 (26.9)	43.3 (29.6)	40.2 (26.7)
E_b^c (kJ/mol)	62.9 (47.0)	60.2 (44.4)	38.4 (23.1)	39.0 (23.9)	-	-

FIGURE 6.3: Elbow plot of ammonia on Ru(0001) as a function of Z_N and r (distance between the nitrogen atom and the surface, and the length of the dissociating NH bond, respectively), where other degrees of freedom are fixed according to the top2fcc TS geometry. Contour lines are drawn at intervals of 10 kJ/mol between -40 and 200 kJ/mol. The white circles indicate the MEP and the black square indicates the highest point along the MEP.



6.3 Results

6.3.1 Activation Barriers and Adsorption Energies

Figures 6.2a-c show the top2fcc barrier geometry obtained with the RPBE-vdW-DF1 DF and depicts the angles that are used in the description of the barrier heights and geometries obtained with the RPBE-vdW-DF1, SRP32-vdW[17] and PBE[28] DFs shown in Tables 6.3 and 6.3. The θ_1 angle is the angle between the dissociating bond and the surface normal. The β angle is the angle between the surface normal and the principal axis of the NH_2 fragment, which is defined as the vector going from the geometric center of the two non-dissociating hydrogen atoms to the nitrogen atom. The γ angle indicates the angle between the axis defined and the dissociating bond (see Figure 6.2a). Z_N indicates the distance of the nitrogen atom to the surface and the length of the dissociating NH bond is indicated by r (see Figure 6.2b).

Two barriers have been obtained, the top2fcc and top2hcp barriers, of which the top2hcp barrier height (63.2 kJ/mol) is 2.7 kJ/mol lower than the top2fcc barrier height (65.9 kJ/mol). Moreover, in terms of the five coordinates shown in Figures 6.2a and 6.2b the two barrier geometries are very similar, with an important difference being the location of the dissociating hydrogen atom, i.e., towards the fcc and hcp hollow sites. Additionally, Figure 6.3 shows the elbow plot of ammonia on Ru(0001), where Z_N and r are allowed to vary but the remaining NH_3 coordinates are fixed to the top2fcc TS values. For this geometry, an adsorption well of about 36 kJ/mol is found before the MEP makes a turn. The top2fcc barrier geometry obtained by Hu et al.[26] using the PBE DF is similar to the one obtained with the RPBE-vdW-DF1

DF but their top2fcc barrier height is 20.3 kJ/mol lower. Moreover, with the computational setup described in Section 6.2, but with the PBE DF, a similar top2fcc barrier height and geometry is obtained as Hu et al.[26], where the difference in barrier heights is only 2.3 kJ/mol. Interestingly, for PBE the top2hcp barrier height obtained in this chapter is also lower than the top2fcc barrier height (by 3.1 kJ/mol), but the top2hcp barrier was not mentioned previously by Hu et al.[26]. Nevertheless, the top2hcp barrier is confirmed to be present and to yield the lowest barrier height in the work of Hu et al. as well (private communication). It should also be noted that the converged surface lattice constant for PBE in this work is slightly smaller ($a = 2.7148 \text{ \AA}$) than the one obtained by Hu et al.[26] ($a = 2.7251 \text{ \AA}$) due to Hu et al. employing tetrahedron smearing with Blöchl corrections[51] for the bulk optimization instead of Fermi-Dirac smearing[52], which is employed throughout the rest of their DFT calculations.

With the SRP32-vdW DF previously developed for $\text{CHD}_3 + \text{Ni}(111)$ [17] barrier heights for $\text{NH}_3 + \text{Ru}(0001)$ are obtained that are similar to the PBE barrier heights, although now the top2fcc barrier height is 0.6 kJ/mol lower than the top2hcp barrier height (Tables 6.3 and 6.3). Again, the geometries are similar to the geometries obtained with the RPBE-vdW-DF1 DF. This was also observed for the barriers of CHD_3 on Pt(111) obtained with the PBE and SRP32-vdW DFs[5]. In general, it seems that the vdW interactions mostly lower the barrier height, and do not affect the barrier geometry much: Mixing in repulsive RPBE exchange (by going from PBE to SRP32 or RPBE exchange) while retaining PBE correlation would raise the barrier, but replacing PBE by vdW correlation fully (in case of SRP32 exchange) or partly (for RPBE exchange) compensates for this. However, the inclusion of vdW interactions may affect other areas of the PES in different ways, and therefore the dynamics may change as well, as has been shown for $\text{CHD}_3 + \text{Pt}(111)$ [5].

The adsorption well of ammonia on Ru(0001) is shown in Figure 6.4, which is obtained by fixing the ammonia in the gas phase geometry. It is observed that the adsorption well is considerably deeper when the nitrogen atom points downwards (74.5 kJ/mol) than when the hydrogen atoms point downwards (18.5 kJ/mol), which corresponds to a chemisorbed and physisorbed state, respectively. When the ammonia molecule is fully relaxed at the surface an adsorption energy of 75.7 kJ/mol is obtained (see Table 6.5), which is in reasonable agreement with experiment (88.7 kJ/mol)[53]. Moreover, allowing the surface atoms to relax in response to the molecule as well yields an adsorption energy of 81.4 kJ/mol (Table 6.5), which is in even better agreement with experiment. When also the interaction energy of 3.0 kJ/mol is taken into account due to the employed vacuum distance (see Section 6.2), an adsorption

FIGURE 6.4: Physisorption and chemisorption well of ammonia on Ru(0001). The blue and red lines indicate whether the hydrogen atoms (physisorption) or nitrogen atom (chemisorption) are closest to the surface, respectively. The asymptotic gas phase energy is taken as zero.

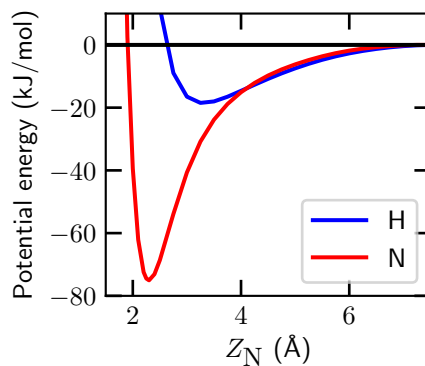


TABLE 6.5: Adsorption energies (E_{ads}) of NH_3 on Ru(0001) computed with the RPBE-vdW-DF1 DF, where the metal surface is kept fixed and relaxed. Ammonia is always relaxed. The corrected adsorption energies due to the interaction energy caused by the smaller vacuum distance are provided in the brackets.

Site	Surface relaxed w.r.t. vacuum		Surface relaxed w.r.t. NH_3	
	Z_{N} (Å)	E_{ads} (kJ/mol)	Z_{N} (Å)	E_{ads} (kJ/mol)
Bridge	2.61	-29.8 (-32.8)	2.55	-32.4 (-35.4)
Fcc	2.75	-26.2 (-29.2)	2.70	-28.1 (-31.1)
Hcp	2.78	-25.6 (-28.6)	2.78	-26.3 (-29.3)
Top	2.30	-75.7 (-78.7)	2.36	-81.4 (-84.4)
T2f	2.34	-50.7 (-53.7)	2.36	-62.1 (-65.1)
T2b	2.32	-56.2 (-59.2)	2.36	-66.6 (-69.6)
Top (PBE)[26]	2.23	-83.7	-	-
Top (Exp.)[53]	-	-	-	-88.7

energy of 84.4 kJ/mol is obtained (Table 6.5), which reproduces the experiment with almost chemical accuracy. With the PBE DF a similar adsorption energy (83.5 kJ/mol)[26] is obtained. This similarity in adsorption energy is attributed to the PBE exchange typically binding more than the RPBE exchange, combined with the vdW correlation compensating for this effect. Furthermore, the preferred adsorption site is the top site, which is in agreement with theory and experiments by Maier et al.[54] and Hu et al.[26], who both used the PBE DF without long-range correlation effects.

The barrier heights computed with the RPBE-vdW-DF1 DF can also be corrected for the unconverged value of the vacuum distance, obtaining E_b^c . Values of E_b^c and the associated zero-point energy corrected values are listed in Tables 6.3 and 6.4.

6.3.2 Sticking Probability

The computed sticking probability of ammonia on Ru(0001) is shown in Figure 6.5a. The sticking probabilities computed by Hu et al. for vibrationally ground state NH_3 [26] and the sticking probabilities measured by Mortensen et al.[25] are also shown. The sticking probability obtained with the RPBE-vdW-DF1 DF for a mobile surface is in better agreement with experiment than the sticking probabilities computed using the PBE DF within the static surface approximation[26]. The computed RPBE-vdW-DF1 sticking probabilities are smaller than the PBE sticking probabilities even though in the calculation of the latter the contribution from excited vibrational states to the sticking was omitted, and no averaging over the velocity distribution in the molecular beam was performed. Performing both averaging procedures would have led to even higher PBE sticking probabilities (see Figure 6.6 for sticking probabilities for vibrationally ground state NH_3). Furthermore, when the experimental results are multiplied with a factor 1.5 (Figure 6.5b), excellent agreement between the computed RPBE-vdW-DF1 and the measured sticking probabilities is obtained. This multiplication improves the mean absolute deviation (the mean of the distances between the theoretical and experimental sticking probability curves along the energy axis) from 23.1 kJ/mol to 4.5 kJ/mol, which is almost within chemical accuracy. Moreover, in agreement with experiment, no difference in reactivity is obtained using a surface temperature of 475 K or 1100 K at high incidence energy, i.e., the sticking probability has no surface temperature dependence. Trapping is also observed (see Figure 6.B.1), but the trapped molecules will most likely desorb when the corresponding trajectories are propagated longer for the incidence energies considered, where the measured sticking is independent of surface temperature.

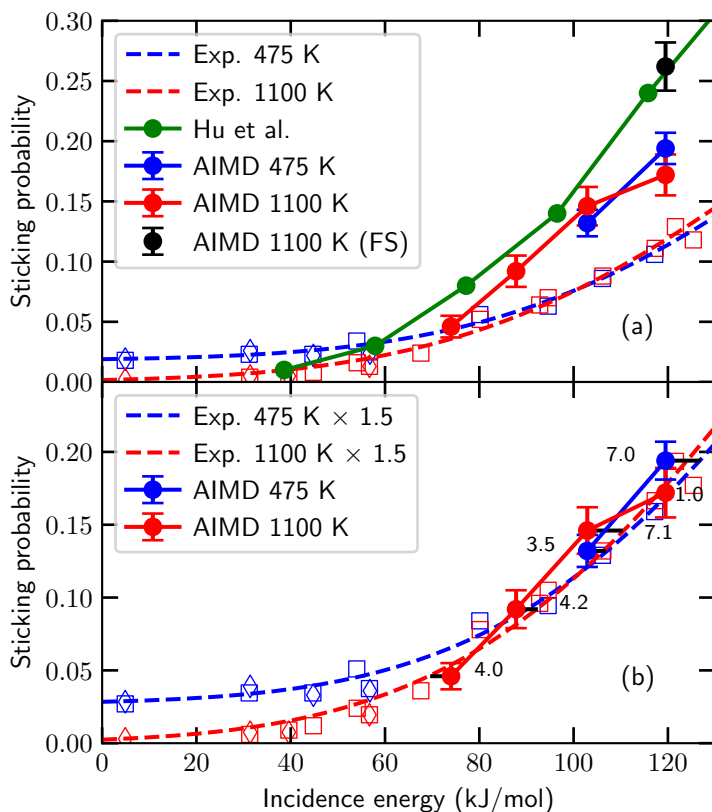


FIGURE 6.5: (a) Sticking probability of ammonia on Ru(0001). All theoretical results are indicated by closed circles and the experimental results are indicated by open diamonds and squares, of which the diamonds and squares are measurements using hydrogen or nitrogen desorption, respectively. Experimental results are taken from Ref. [25], and previous theoretical results without surface motion (closed green circles) are from Ref. [26]. The AIMD results are the closed blue ($T_s = 475$ K) and red ($T_s = 1100$ K) circles. The error bars represent 68% confidence intervals. (b) Same as panel a, but with the experimental results multiplied with a factor 1.5. The horizontal offsets between the computed and fitted experimental sticking probabilities are indicated by the numbers (in kJ/mol).

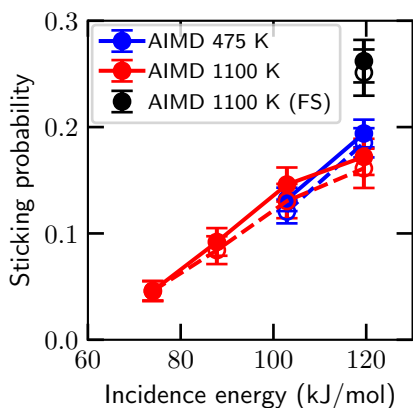


FIGURE 6.6: Sticking probability of NH_3 on Ru(0001). Theoretical results including vibrational states sampled with a Boltzmann distribution according to T_n or only the ground state are indicated by closed and open circles, respectively. $T_s = 475$ K and 1100 K with(out) surface motion are represented by the blue and red (black) symbols, respectively. The error bars represent 68% confidence intervals.

The effect of surface motion is investigated as well by fixing the surface atoms in their ideal positions, commonly referred to as a frozen surface or Born-Oppenheimer static surface model, but using a lattice expansion coefficient corresponding to $T_s = 1100$ K. This excludes any energy transfer from ammonia to the surface atoms, and corrugation in barrier heights and positions due to the movement of the surface atoms. In Figure 6.5a the sticking probability on the frozen surface is considerably higher than on the mobile surface. The thermal modulation of barrier heights and positions typically has a negligible effect on the sticking probability when the incidence energy is near or above the barrier height, as has been shown previously for methane reacting on several surfaces[8, 55, 56]. Furthermore, since both in this work and the experiments performed by Mortensen et al.[25] no surface temperature dependence is found for the incidence energies addressed, it is expected that this holds true for $\text{NH}_3 + \text{Ru}(0001)$ as well. Therefore, it is likely that the increase in sticking is mainly caused by the lack of energy transfer from the molecule to the surface atoms, and thus including surface motion into the modeling of $\text{NH}_3 + \text{Ru}(0001)$ is necessary.

The difference between the computed sticking probabilities in this chapter and those by Hu et al.[26] for vibrationally ground state ammonia is somewhat smaller than might have been expected from the difference between the E_b value of PBE (45.6 kJ/mol)[26] and RPBE-vdW-DF1 (62.9 kJ/mol). However, note that the sticking probability of Hu et al. should be underestimated as also the contribution of vibrationally excited NH_3 should be taken into account (see Figure 6.6). Furthermore, as will be shown in the next section, the dynamics plays an important role in the dissociation of ammonia, especially the re-orientation of ammonia. Therefore, the minimum barrier height might play a

TABLE 6.6: Average value of the θ_1 , β and γ angles with the standard error (σ_m) and standard deviation (σ) for all reacted and scattered trajectories. The top2fcc and top2hcp TS values are included as well.

	$\theta_1(^{\circ}) \pm \sigma_m(\sigma)$	$\beta(^{\circ}) \pm \sigma_m(\sigma)$	$\gamma(^{\circ}) \pm \sigma_m(\sigma)$
Reacted ($t = 0$)	41.0 ± 1.1 (25.5)	62.2 ± 1.1 (26.6)	62.3 ± 0.4 (9.8)
Reacted ($r = r^{\ddagger}$)	103.6 ± 0.5 (12.5)	155.2 ± 0.6 (13.4)	74.6 ± 0.8 (19.1)
Scattered ($t = 0$)	89.7 ± 0.7 (38.4)	90.6 ± 0.7 (40.1)	62.2 ± 0.2 (9.8)
top2fcc	115.6	177.2	61.6
top2hcp	116.1	176.5	60.3

smaller role than expected.

The sticking probabilities measured on Ru(0001) were not absolute sticking probabilities, but relative sticking probabilities measured by a combination of three different methods using partial pressures and temperature programmed desorption (TPD) of H₂ and N₂. The relative sensitivities of these three methods were calibrated to one another for overlapping regimes of surface temperatures where the methods were applicable. Absolute sticking probabilities were then obtained by also performing a King and Wells experiment[57] on a surface with an artificially high defect concentration created by sputtering, against which the other methods for measuring sticking of NH₃ on defect free Ru(0001) were then calibrated[25]. This procedure was needed due to the tendency of NH₃ to stick to the walls of the chamber. However, the uncertainty of the absolute sticking probabilities obtained in this manner was not stated. Since the shape of the sticking probability curve is predicted correctly if the experimental data is multiplied with a factor 1.5 (see Figure 6.5b), and the experimental error margin is unknown, it is possible that the disagreement between experiment and theory in this chapter is at least in part caused by an error in the calibration of the sticking probabilities. On the other hand, the results of Chapter 5 suggest that a GGA DF will always underestimate the barrier height of NH₃ + Ru(0001) since the difference between the molecule's electron affinity and the metal surface's work function is smaller than 7 eV, thus likely requiring a DF that reduces the self-interaction error (e.g., a screened hybrid DF). Nevertheless, additional experiments are required in order to validate both theory and experiment. For further discussion of the agreement between theory and experiment, see Section 6.4.

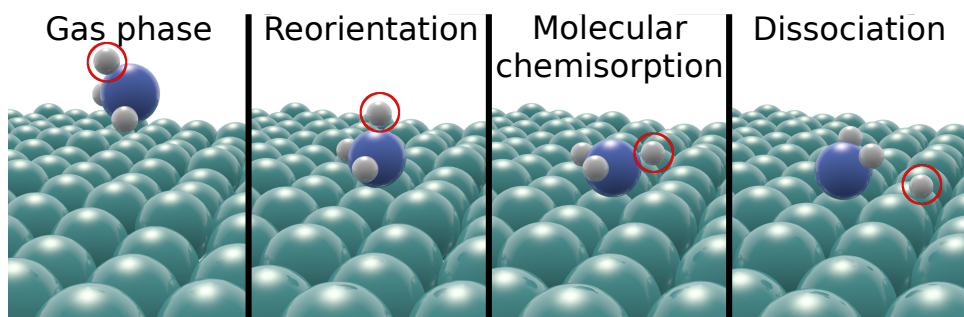


FIGURE 6.7: Snapshots from a typical trajectory of reacting ammonia on Ru(0001). The gas phase (a), first moment of reorientation (b), molecular chemisorbed state (c), and moment of reaction (d) are depicted. The dissociating hydrogen atom is indicated by the red circles. The simulation time portrayed in these panels is about 50 fs.

6.3.3 Dynamics During the Reaction

In order to elucidate the reaction mechanism of ammonia on Ru(0001), the dynamics of the reaction is now investigated. First, all reacted trajectories, except for one, occurred without bouncing, so the reaction proceeds directly, without the system going through a long-lived molecular precursor state. However, looking at the angles of ammonia during a reaction (see Figure 6.1, Table 6.6, and Figures 6.7a-d, which present snapshots from a representative example of the reactive trajectories) paints a different picture. The initial distribution of θ_1 is centered on values smaller than 90° (Figure 6.1b), so typically the leaving H atom initially points away from the surface (Figure 6.7a). The dissociating hydrogen atom is only reoriented towards the surface (as in the TS, see Figure 6.2a) near the moment of the reaction (i.e., when $r = r^\ddagger$), see Figures 6.1b and 6.7d. Moreover, the non-dissociating hydrogen atoms are initially oriented towards the surface ($\theta_{2,3} > 90^\circ$ and $\beta < 90^\circ$, Figures 6.1c,d and 6.7a), while at the time of reaction they point upwards ($\theta_{2,3} < 90^\circ$ and $\beta > 90^\circ$, Figures 6.1c,d and 6.7d). Closer inspection of the reacted trajectories suggests that the nitrogen atom first binds to the surface (Figures 6.7b and 6.7c), while the two non-dissociating hydrogen atoms are oriented along (Figure 6.7b) and then away from (Figure 6.7c) the surface. After this, a rapid reorientation of all hydrogen atoms occurs and subsequently a hydrogen atom dissociates (Figure 6.7d), which is the hydrogen atom that was originally oriented away from the surface (Figure 6.7a). It is possible that by first binding the nitrogen atom to the surface, and thus forming a chemisorbed molecule, the NH bond is destabilized so that it can dissociate more easily after reorientation. Furthermore, this reaction occurs rapidly and without

bounces on the surface, where typically the time between ammonia impacting on the surface and dissociation of an NH bond is about 50 to 150 fs. Several movies of dissociation events are provided in the supporting information of Ref. [58] to illustrate the mechanism. Since the dissociative chemisorption of ammonia on Ru(0001) occurs initially through molecular chemisorption and only subsequently an NH bond dissociates, this is arguably not a simple direct reaction mechanism as reported before [25, 26], but rather a molecular chemisorption mediated direct reaction mechanism.

Importantly, at the initial time step the orientation distribution of the reacting molecule is non-statistical, i.e., it does not resemble a $\sin(\theta)$ distribution as shown in Figure 6.1a. A non-statistical initial distribution has also been observed for other polyatomic molecules reacting on metal surfaces (Figure 6.1a) (e.g., CHD₃ [15, 17, 50] and methanol [7], see Chapters 7, 9 and 10) for which cases the reaction mechanism can be described reasonably well as a rotational sudden mechanism. Interestingly, unlike for the aforementioned cases, the initial orientation distribution of NH₃ does not resemble the barrier geometry or the orientation distribution at the time of reaction. Only at the moment of dissociation, i.e., when $r = r^\ddagger$ for the dissociating bond, does the time-evolved orientation distribution of ammonia resemble the barrier geometry, which to the best of our knowledge has not been observed before. This has consequences for the approximations that can be made in modeling the reaction. For example, the HOD + Ni(111) reaction can be treated as rotationally adiabatic [4, 59], while the reaction of CHD₃ + Ni(111) can be treated reasonably well with a rotational sudden approximation [14] (see also Figure 6.1a). However, the unique behaviour of ammonia, where rotationally non-adiabatic dynamics is coupled with a non-statistical distribution of the orientation of the reacting molecule at $t = 0$, prevents the usage of such approximations and only models where the full dynamics is included, such as AIMD, can describe NH₃ + Ru(0001) correctly. It should be noted that although HCl + Au(111) appears to exhibit a statistical initial distribution and a time-evolved distribution of the orientation of HCl resembling the barrier geometry (i.e., a rotational adiabatic mechanism, see Chapter 3), a careful analysis of the reaction mechanism suggests that the reaction is, in fact, rotationally non-adiabatic, similar to NH₃ + Ru(0001) (see Chapter 4). Furthermore, quantum dynamics might be necessary to describe the reaction of NH₃ on Ru(0001) [26] at low E_i , but performing quantum dynamics (QD) calculations using the full 12D hamiltonian is probably computationally prohibitive. So far QD employing a hamiltonian including all degrees of freedom of the molecule has been performed up to 9D, e.g., on H₂O + Cu(111) [60]. For molecule-surface systems with more than nine molecular degrees of freedom reduced dimensionality

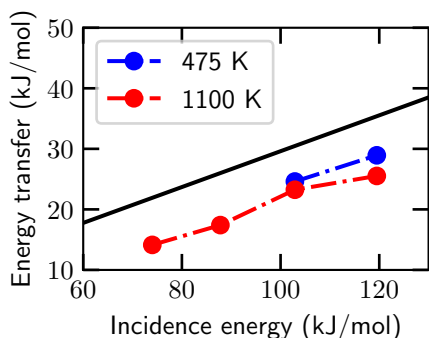


FIGURE 6.8: Average energy transfer from scattered ammonia to Ru(0001) compared to the refined Baule model. The black line is the energy transfer predicted by the refined Baule model, whereas the blue and red circles indicate the energy transfer predicted by AIMD at $T_s = 475$ K and 1100 K, respectively.

hamiltonians have been employed, e.g., with nine degrees of freedom for $\text{CH}_4 + \text{Ni}(111)$ [61], and the use of the rotationally adiabatic or rotational sudden approximation might therefore be desirable. However, as has been noted here, these approximations are not valid for the reaction of NH_3 on Ru(0001), and therefore employing a reduced dimensionality hamiltonian may not be straightforward.

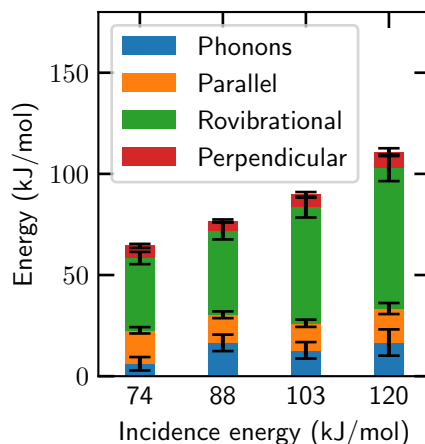
Figure 6.8 shows the predicted energy transfer of the scattered trajectories obtained with AIMD and by the refined Baule model[62, 63] (see also Section 2.5), which is defined as

$$\langle E_T \rangle = \frac{2.4\mu}{(1 + \mu)^2} \langle E_i \rangle, \quad (6.2)$$

where $\mu = m/M$ (m is the mass of ammonia and M is the mass of a ruthenium atom) and $\langle E_i \rangle$ is the average incidence energy. Here it is seen that the energy transfer computed with AIMD is about 20%, whereas the refined Baule model predicts an energy transfer of about 30%. This disagreement is larger than has generally been observed for CHD_3 [63] (Chapter 9) and methanol[7] (Chapter 10). It is possible that trajectories that transfer less energy from ammonia to the metal surface are also less likely to trap, and therefore that the average energy transfer is lower than one would expect from the comparatively simple refined Baule model.

Molecules are most likely to trap when the lone pair on the nitrogen atom is pointing away from the surface ($\beta' < 90^\circ$, see Figure 6.1e). When the lone pair is oriented more towards the surface, it is considerably more likely to react, probably due to the possibility of forming the chemisorption-like state required for the reaction. An obvious reason for trapping would be the translational energy transfer from the ammonia to the metal surface.

FIGURE 6.9: Kinetic energy of trapped ammonia parallel (XY direction, orange) and perpendicular (Z direction, red) to the surface, the energy transferred from NH_3 to the surface phonons (compared to $t = 0$, blue), and increase in the rovibrational energy of NH_3 (compared to $t = 0$, green) at the final time step, i.e., when $t = 1.0$ ps, as a function of incidence energy. The error bars represent 68% confidence intervals.



However, even when energy transfer from the molecule to the surface is not allowed by employing a frozen surface, trapping is still observed (about 2% at $\langle E_i \rangle = 119$ kJ/mol, versus 5% if surface motion is included, see Figure 6.B.1). This suggests that energy transfer to other motions, i.e., motions of NH_3 , may also cause ammonia to be trapped. For instance, it is possible to excite the vibrational bending mode of ammonia when the umbrella is pointing towards the surface, thereby converting translational energy into vibrational energy. Also, a large fraction of the translational energy of trapped molecules is oriented parallel to the surface instead of perpendicular to the surface after the initial collision. These energy transfer effects are quantified in Figure 6.9. The largest energy transfer is observed to vibrations and rotations, and this represents about 60% of the energy transferred. The energy transfer from motion normal to the surface to motion parallel to the surface and to the phonons and rovibrational motion make it less likely to scatter. It is expected that these trapped trajectories are likely to scatter back into the gas phase at longer simulation times, as they might be able at some point to escape both the chemisorption and physisorption wells. This has also been observed for some of the scattered trajectories, which scattered after one or two bounces on the surface. The observation of trajectories that scattered after one or two bounces, and the observation that only one of the reacted trajectories was indirect (occurred with bouncing) is in accordance with the original proposal by the experimentalists[25] of a direct mechanism for the high E_i addressed here, and the surface temperature independence of reaction they observed.

Figure 6.10 shows that the reaction occurs relatively more near (i.e., more than expected on the basis of relative surface areas) the bridge site than near

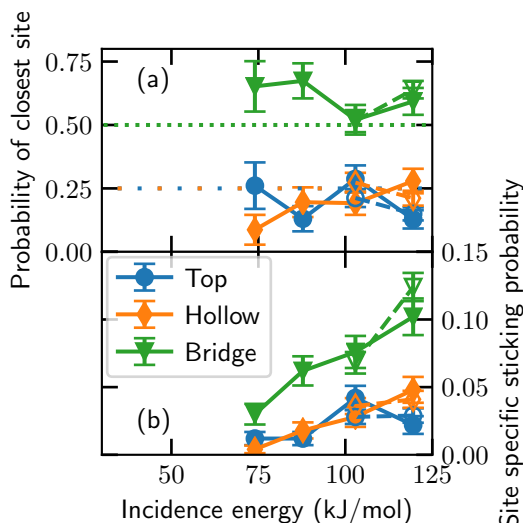


FIGURE 6.10: (a) Fraction of closest high symmetry site, i.e., the top, hollow and bridge (blue, orange and green, respectively) sites, to the impact site of reacting ammonia as a function of the incidence energy when a bond dissociates, i.e., when $r = r^\ddagger$. The open and closed symbols indicate a surface temperature of 475 K and 1100 K, respectively. The dotted lines indicate the statistical average for the high symmetry sites. (b) The sticking probability of NH_3 on the high symmetry sites as a function of the incidence energy. The error bars represent 68% confidence intervals.

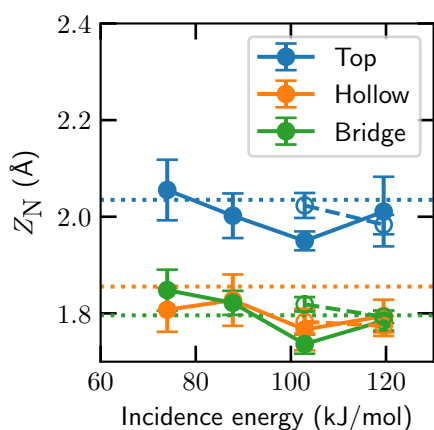
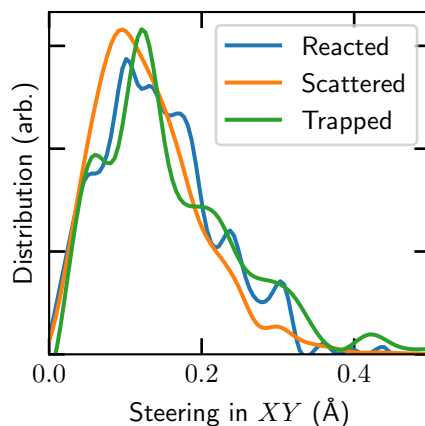


FIGURE 6.11: Distance of the nitrogen atom to the surface when a bond dissociates, i.e., when $r = r^\ddagger$, as a function of incidence energy. The open and closed circles indicate a surface temperature of 475 K and 1100 K, respectively. The blue, orange, and green lines indicate the top, hollow, and bridge sites. The horizontal dotted lines indicate the TS values of Z_N , where the values belonging to the hollow and bridge sites are taken from Ref. [26]. The error bars represent 68% confidence intervals.

FIGURE 6.12: Distribution of steering of ammonia in the XY direction for all reacted (blue), scattered (orange) and trapped (green) trajectories. Steering is here defined as the distance travelled by NH_3 in the XY plane between the initial time step and first classical turning point for the scattered and trapped trajectories, and between the initial time step and when a bond dissociates, i.e., when $r = r^\ddagger$, for reacted trajectories.



the top and hollow sites. However, from the minimum barrier location (near the top site, see Section 6.3.1) one would expect that the top site should be relatively more reactive than the other sites. The barrier height on the bridge site was predicted by Hu et al. to be 11 kJ/mol higher than the minimum barrier height[26]. Furthermore, the reactivity of the top and hollow sites is similar, even though compared to the minimum barrier the barriers on the hcp and fcc sites were predicted to be higher by 49 and 38 kJ/mol, respectively[26]. The possibility is considered here that the relatively low reactivity near the top site is caused by the bobsled effect[64, 65], which can reduce the reactivity as it causes the molecule to slide off the MEP and react over a higher barrier than the lowest barrier[8, 63]. However, Figure 6.11 shows that the average distance of the nitrogen atom to the surface is close to the TS value for all three sites. Therefore, it seems unlikely that the bobsled effect plays a large role. At present, it remains unclear why the bridge site is more reactive than the top and hollow sites. It can be speculated that the use of vdW-DF1 correlation leads to the barriers being relatively lower (i.e., compared to PBE) above the bridge and hollow sites, where the barriers are closer to the surface.

Interestingly, a considerable amount of steering in the XY plane is observed (see Figure 6.12). The steering also seems to be independent of incidence energy and whether the trajectory will go on to react, scatter or trap. Moreover, looking at Figure 6.13, the dynamical steering in the XY direction mostly steers the ammonia away from the hollow sites towards the bridge sites. At high incidence energy steering from the bridge site towards the top site occurs as well.

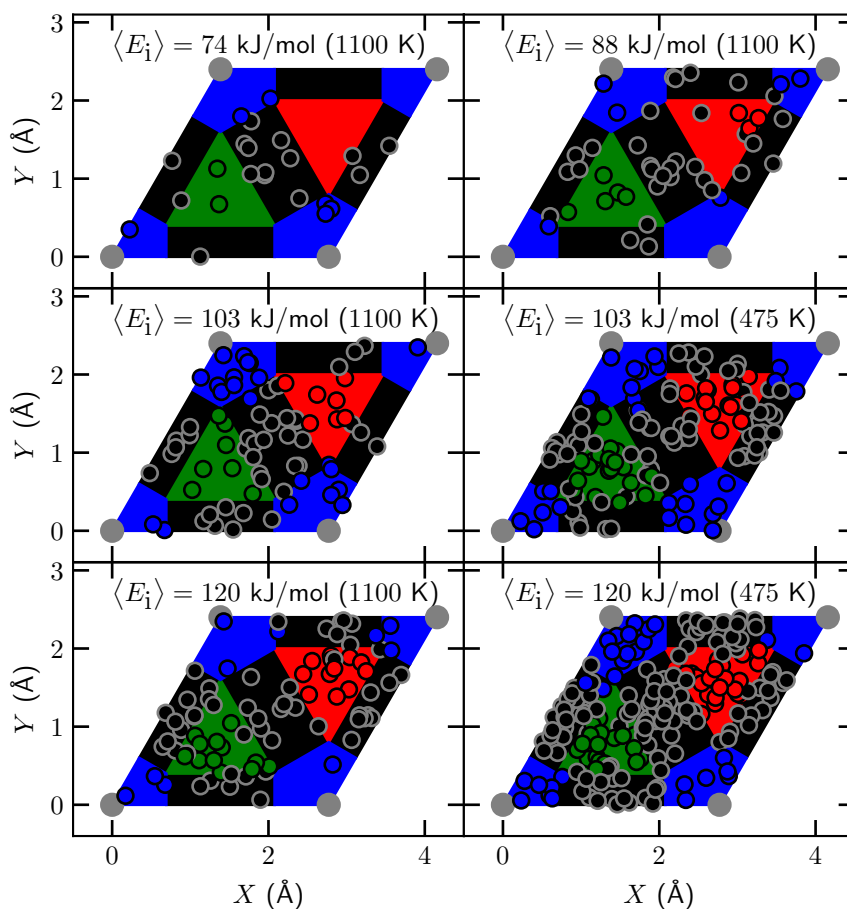


FIGURE 6.13: Impact site of reacting ammonia on Ru(0001) indicated with circles at the initial time step, i.e., $t = 0$ fs and $Z_{\text{COM}} = 7.5 \text{ \AA}$, whereas the color of the circle indicates the closest high symmetry site when a bond dissociates, i.e., when $r = r^\ddagger$. The top, fcc, hcp and bridge sites are indicated in blue, green, red and black, respectively, and the top layer atoms are indicate by the gray circles.

6.4 Discussion of the Comparison of Experiment and Theory

Here, potential issues are discussed with both theory and experiment that could further affect the comparison between the measured and computed reaction probabilities. First, the inversion of the umbrella of the ammonia molecule during the dynamics might be treated incorrectly with the QCT approach in the AIMD[66, 67]. Especially when higher nozzle temperatures are employed, the probability of having vibrationally excited bending modes is considerable. However, in the AIMD the inversion of the umbrella does not occur before reaching the surface, and the inversion of ammonia occurs on a timescale (once per 21 ps[68]) that is considerably longer than the time it takes to reach the surface in the AIMD (100 fs). Therefore, it is concluded that the QCT approach should be valid at high incidence energies where reaction occurs in a "classical over the barrier fashion", and thus tunneling should not play a significant role. Another issue is that the experimental beam parameters[25] are not exactly known, making a direct quantitative comparison difficult as beam parameters can have a large effect on the reaction probability of molecules reacting on metal surfaces[30, 69, 70]. This effect can also be seen in Figure 6.6 where results are compared for ammonia in the vibrational ground state with ammonia vibrationally excited according to a Boltzmann distribution. At the higher incidence energies and concomitant higher nozzle temperatures, the sticking probability of vibrational ground state ammonia is somewhat lower than when the vibrational excitations in the molecular beam are taken into account.

6.5 Conclusions

In this chapter the dissociative chemisorption of ammonia on Ru(0001) is investigated with AIMD. Not only is surface motion included for this reaction for the first time, a DF incorporating attractive Van der Waals correlation (RPBE-vdW-DF1) is employed as well. With respect to earlier work employing the PBE DF and modeling the Ru(0001) surface as static the computed sticking probability is found to be in improved agreement with experiment. This improvement is attributed to both modeling the Ru(0001) as a mobile surface, and using the RPBE-vdW-DF1 DF. Also, the lack of surface temperature dependence at high incidence energy observed by experiment is confirmed with AIMD. It is found that the modeling of surface motion is required to accurately describe the sticking probability. The reaction mechanism is neither

rotationally adiabatic nor rotational sudden, with initial and intermediate (i.e., at time of reaction) orientation distributions that are both non-statistical, but do not resemble one another, which to the best of our knowledge has not been observed before. Furthermore, it is observed that under the conditions investigated the dissociation of ammonia on Ru(0001) is not described by a simple direct, or by an indirect trapping-mediated reaction mechanism, but rather by a direct reaction mechanism in which NH_3 goes through a very short-lived molecularly chemisorbed state. Direct dissociative chemisorption of a polyatomic molecule where the molecular chemisorption of a molecule is immediately followed by dissociation has also not been observed before.

Appendix

6.A Convergence

Figure 6.A.1 and Table 6.A.1 illustrate the convergence of the minimum barrier height for ammonia dissociation on Ru(0001) (E_b) as a function of number of layers for different numbers of k -points using a kinetic energy cut-off of 400 eV, yielding a converged barrier height of 44.8 kJ/mol. The SRP32-vdW DF that was originally developed for $\text{CHD}_3 + \text{Ni}(111)$ [17] is used here instead of the RPBE-vdW-DF1 DF used throughout the rest of this chapter. Moreover, a vacuum distance of 13 Å is used, instead of 15 Å used in the rest of this chapter. However, similar convergence behaviour is expected. The computational set up employed for the AIMD calculations (4 layers, 3×3 surface unit cell, $4 \times 4 \times 1$ k -points, kinetic energy cut-off of 400 eV), with the exception noted for the vacuum distance, gave a barrier height of 44.0 kJ/mol. It is confirmed that the computational set up is also converged with respect to the kinetic energy cut-off. Furthermore, Table 6.A.2 shows the top2hcp barrier heights obtained with the SRP32-vdW DF as a function of the vacuum distance. Here it can be seen that 30 Å yields converged barrier heights. Note that in Table 6.A.2 for only a vacuum distance of 13 and 30 Å a dimer calculation is performed, whereas for the other values of the vacuum distance the barrier geometry yielded by 13 Å is employed, i.e., a so-called single point calculation is performed. For a vacuum distance of 30 Å it is confirmed that a single point calculation reproduces the result of the dimer calculation. However, for 15 Å a small difference of 1.4 kJ/mol is obtained between the single point and dimer calculations (see Table 6.3, where $E_b = 42.0$ kJ/mol instead of 40.6 kJ/mol). Hence, a translational energy shift of 4.4 kJ/mol instead of 3.0 kJ/mol would have been more appropriate due to the interaction energy (see Section 6.2), but we consider this difference to be small enough to not affect the results presented in this chapter considerably. It is also confirmed that employing the RPBE-vdW-DF1 DF yields the same difference in barrier heights between 15 Å and 30 Å as the SRP32-vdW DF.

TABLE 6.A.1: Convergence of the minimum barrier height (kJ/mol) on Ru(0001) (top2hcp geometry) is shown as a function of the amount of layers, k -points, and the size of the surface unit cell (3×3 and 4×4) for a plane wave energy cutoff of 400 eV using the SRP32-vdW DF. A vacuum distance of 13 Å instead of 15 Å (used throughout the rest of this chapter) is employed. The results obtained with the employed computational set up in the AIMD (except the vacuum distance) is in bold and the most converged result (i.e., obtained with the largest setup) is in italic.

Layers	k -points	$E_b, 3 \times 3$	$E_b, 4 \times 4$
4	$3 \times 3 \times 1$		44.0
4	$4 \times 4 \times 1$	44.0	42.2
4	$6 \times 6 \times 1$	43.5	42.8
4	$8 \times 8 \times 1$	42.9	42.8
4	$10 \times 10 \times 1$	42.9	
5	$3 \times 3 \times 1$		46.0
5	$4 \times 4 \times 1$	46.6	45.8
5	$6 \times 6 \times 1$	45.7	45.7
5	$8 \times 8 \times 1$	46.3	45.3
5	$10 \times 10 \times 1$	46.2	
6	$3 \times 3 \times 1$		48.2
6	$4 \times 4 \times 1$	47.9	46.8
6	$6 \times 6 \times 1$	47.5	47.5
6	$8 \times 8 \times 1$	47.4	47.4
6	$10 \times 10 \times 1$	47.3	
7	$3 \times 3 \times 1$		46.1
7	$4 \times 4 \times 1$	45.8	45.9
7	$6 \times 6 \times 1$	45.3	45.5
7	$8 \times 8 \times 1$	45.3	45.6
7	$10 \times 10 \times 1$	45.6	
8	$3 \times 3 \times 1$		44.7
8	$4 \times 4 \times 1$	45.1	45.1
8	$6 \times 6 \times 1$	45.3	44.8
8	$8 \times 8 \times 1$	45.2	44.5
8	$10 \times 10 \times 1$	44.9	
9	$3 \times 3 \times 1$		43.9
9	$4 \times 4 \times 1$	44.0	44.3
9	$6 \times 6 \times 1$	44.1	43.8
9	$8 \times 8 \times 1$	43.9	43.6
9	$10 \times 10 \times 1$	43.7	
10	$3 \times 3 \times 1$		44.8
10	$4 \times 4 \times 1$	44.6	44.9
10	$6 \times 6 \times 1$	44.9	45.0
10	$8 \times 8 \times 1$	44.6	44.8
10	$10 \times 10 \times 1$	44.6	

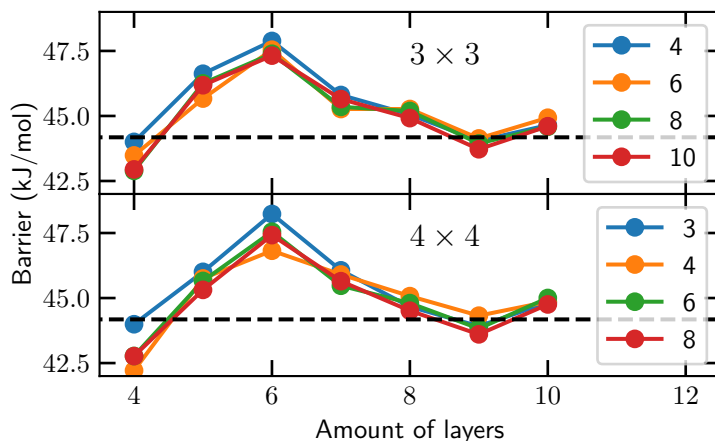
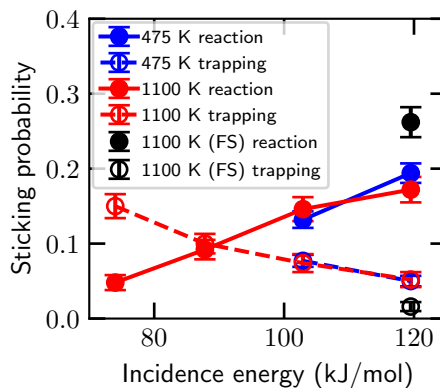


FIGURE 6.A.1: Convergence of the minimum barrier height on Ru(0001) (top2hcp geometry) as a function of the amount of layers for the number of k -points equal to $(n \times n \times 1)$, where n is indicated in the legend. The SRP32-vdW DF is used. The upper panel and lower panel used a 3×3 and 4×4 supercell, respectively. The dashed lines indicate the converged barrier height.

TABLE 6.A.2: Minimum barrier height (kJ/mol) on Ru(0001) (top2hcp geometry) is shown as a function of the vacuum distance with the computational set up used in the AIMD employing the SRP32-vdW DF.

Vacuum distance	E_b (kJ/mol)
13	44.0
15	40.6
17	39.0
20	38.2
25	37.7
30	37.5

FIGURE 6.B.1: Sticking probability of ammonia on Ru(0001) obtained with AIMD. $T_s = 475$ K and 1100 K are represented by the blue and red symbols, respectively. The closed and open symbols indicate reaction probabilities and trapping probabilities, respectively. The error bars represent 68% confidence intervals.



6.B Trapping

Figure 6.B.1 shows the reaction probabilities of NH_3 on Ru(0001) obtained with AIMD, where the trapping probabilities are shown as well. At the lowest incidence energy about three times as much trapping occurs as reaction, whereas at the highest incidence energy the trapping probability is about a factor 4 smaller than the reaction probability. Under the conditions shown in Figure 6.B.1, trapping is not expected to contribute to reaction[25]. If trapping were to affect the reaction probability, it is expected the measured sticking probability to depend on T_s , while it does not.

References

- (1) Lin, X.; Yoon, Y.; Petrik, N. G.; Li, Z.; Wang, Z.-T.; Glezakou, V.-A.; Kay, B. D.; Lyubinetsky, I.; Kimmel, G. A.; Rousseau, R.; Dohnálek, Z. Structure and Dynamics of CO₂ on Rutile TiO₂(110)-1x1. *J. Phys. Chem. C* **2012**, *116*, 26322–26334, DOI: [10.1021/jp308061j](https://doi.org/10.1021/jp308061j).
- (2) Naderian, M.; Groß, A. From Single Molecules to Water Networks: Dynamics of Water Adsorption on Pt(111). *J. Chem. Phys.* **2016**, *145*, 094703, DOI: [10.1063/1.4961870](https://doi.org/10.1063/1.4961870).
- (3) Zhou, X.; Kolb, B.; Luo, X.; Guo, H.; Jiang, B. Ab Initio Molecular Dynamics Study of Dissociative Chemisorption and Scattering of CO₂ on Ni(100): Reactivity, Energy Transfer, Steering Dynamics, and Lattice Effects. *J. Phys. Chem. C* **2017**, *121*, 5594–5602, DOI: [10.1021/acs.jpcc.6b12686](https://doi.org/10.1021/acs.jpcc.6b12686).
- (4) Migliorini, D.; Nattino, F.; Tiwari, A. K.; Kroes, G.-J. HOD on Ni(111): Ab Initio Molecular Dynamics Prediction of Molecular Beam Experiments. *J. Chem. Phys.* **2018**, *149*, 244706, DOI: [10.1063/1.5059357](https://doi.org/10.1063/1.5059357).
- (5) Chadwick, H.; Migliorini, D.; Kroes, G. J. CHD₃ Dissociation on Pt(111): A Comparison of the Reaction Dynamics Based on the PBE Functional and on a Specific Reaction Parameter Functional. *J. Chem. Phys.* **2018**, *149*, 044701, DOI: [10.1063/1.5039458](https://doi.org/10.1063/1.5039458).
- (6) Migliorini, D.; Chadwick, H.; Kroes, G.-J. Methane on a Stepped Surface: Dynamical Insights on the Dissociation of CHD₃ on Pt(111) and Pt(211). *J. Chem. Phys.* **2018**, *149*, 094701, DOI: [10.1063/1.5046065](https://doi.org/10.1063/1.5046065).
- (7) Gerrits, N.; Kroes, G.-J. An AIMD Study of Dissociative Chemisorption of Methanol on Cu(111) with Implications for Formaldehyde Formation. *J. Chem. Phys.* **2019**, *150*, 024706, DOI: [10.1063/1.5070129](https://doi.org/10.1063/1.5070129).
- (8) Gerrits, N.; Shakouri, K.; Behler, J.; Kroes, G.-J. Accurate Probabilities for Highly Activated Reaction of Polyatomic Molecules on Surfaces Using a High-Dimensional Neural Network Potential: CHD₃ + Cu(111). *J. Phys. Chem. Lett.* **2019**, *10*, 1763–1768, DOI: [10.1021/acs.jpcllett.9b00560](https://doi.org/10.1021/acs.jpcllett.9b00560).
- (9) Zhang, Y.; Zhou, X.; Jiang, B. Bridging the Gap between Direct Dynamics and Globally Accurate Reactive Potential Energy Surfaces Using Neural Networks. *J. Phys. Chem. Lett.* **2019**, *10*, 1185–1191, DOI: [10.1021/acs.jpcllett.9b00085](https://doi.org/10.1021/acs.jpcllett.9b00085).

- (10) Farjamnia, A.; Jackson, B. The Dissociative Chemisorption of Water on Ni(111): Mode- and Bond-Selective Chemistry on Metal Surfaces. *J. Chem. Phys.* **2015**, *142*, 234705, DOI: [10.1063/1.4922625](https://doi.org/10.1063/1.4922625).
- (11) Jiang, B. Rotational and Steric Effects in Water Dissociative Chemisorption on Ni(111). *Chem. Sci.* **2017**, *8*, 6662–6669, DOI: [10.1039/C7SC02659E](https://doi.org/10.1039/C7SC02659E).
- (12) Campbell, V. L.; Chen, N.; Guo, H.; Jackson, B.; Utz, A. L. Substrate Vibrations as Promoters of Chemical Reactivity on Metal Surfaces. *J. Phys. Chem. A* **2015**, *119*, 12434–12441, DOI: [10.1021/acs.jpca.5b07873](https://doi.org/10.1021/acs.jpca.5b07873).
- (13) Guo, H.; Farjamnia, A.; Jackson, B. Effects of Lattice Motion on Dissociative Chemisorption: Toward a Rigorous Comparison of Theory with Molecular Beam Experiments. *J. Phys. Chem. Lett.* **2016**, *7*, 4576–4584, DOI: [10.1021/acs.jpcllett.6b01948](https://doi.org/10.1021/acs.jpcllett.6b01948).
- (14) Jackson, B.; Nattino, F.; Kroes, G.-J. Dissociative Chemisorption of Methane on Metal Surfaces: Tests of Dynamical Assumptions Using Quantum Models and Ab Initio Molecular Dynamics. *J. Chem. Phys.* **2014**, *141*, 054102, DOI: [10.1063/1.4891327](https://doi.org/10.1063/1.4891327).
- (15) Gerrits, N.; Migliorini, D.; Kroes, G.-J. Dissociation of CHD₃ on Cu(111), Cu(211), and Single Atom Alloys of Cu(111). *J. Chem. Phys.* **2018**, *149*, 224701, DOI: [10.1063/1.5053990](https://doi.org/10.1063/1.5053990).
- (16) Jackson, B.; Nave, S. The Dissociative Chemisorption of Methane on Ni(100): Reaction Path Description of Mode-Selective Chemistry. *J. Chem. Phys.* **2011**, *135*, 114701, DOI: [10.1063/1.3634073](https://doi.org/10.1063/1.3634073).
- (17) Nattino, F.; Migliorini, D.; Kroes, G.-J.; Dombrowski, E.; High, E. A.; Killelea, D. R.; Utz, A. L. Chemically Accurate Simulation of a Polyatomic Molecule-Metal Surface Reaction. *J. Phys. Chem. Lett.* **2016**, *7*, 2402–2406, DOI: [10.1021/acs.jpcllett.6b01022](https://doi.org/10.1021/acs.jpcllett.6b01022).
- (18) Ertl, G. Primary Steps in Catalytic Synthesis of Ammonia. *J. Vac. Sci. Technol. A* **1983**, *1*, 1247–1253, DOI: [10.1116/1.572299](https://doi.org/10.1116/1.572299).
- (19) Nielsen, A., *Ammonia: Catalysis and Manufacture*; Springer Science & Business Media: 2012; 352 pp.
- (20) Erisman, J. W.; Sutton, M. A.; Galloway, J.; Klimont, Z.; Winiwarter, W. How a Century of Ammonia Synthesis Changed the World. *Nat. Geosci.* **2008**, *1*, 636–639, DOI: [10.1038/ngeo325](https://doi.org/10.1038/ngeo325).

- (21) Choudhary, T.; Sivadinarayana, C.; Goodman, D. Catalytic Ammonia Decomposition: CO_x-Free Hydrogen Production for Fuel Cell Applications. *Catal. Lett.* **2001**, *72*, 197–201, DOI: [10.1023/A:1009023825549](https://doi.org/10.1023/A:1009023825549).
- (22) Schüth, F.; Palkovits, R.; Schlögl, R.; Su, D. S. Ammonia as a Possible Element in an Energy Infrastructure: Catalysts for Ammonia Decomposition. *Energy Environ. Sci.* **2012**, *5*, 6278–6289, DOI: [10.1039/C2EE02865D](https://doi.org/10.1039/C2EE02865D).
- (23) Mukherjee, S.; Devaguptapu, S. V.; Sviripa, A.; Lund, C. R. F.; Wu, G. Low-Temperature Ammonia Decomposition Catalysts for Hydrogen Generation. *Appl. Catal. B* **2018**, *226*, 162–181, DOI: [10.1016/j.apcatb.2017.12.039](https://doi.org/10.1016/j.apcatb.2017.12.039).
- (24) Bradford, M. C. J.; Fanning, P. E.; Vannice, M. A. Kinetics of NH₃ Decomposition over Well Dispersed Ru. *J. Catal.* **1997**, *172*, 479–484, DOI: [10.1006/jcat.1997.1877](https://doi.org/10.1006/jcat.1997.1877).
- (25) Mortensen, H.; Diekhöner, L.; Baurichter, A.; Jensen, E.; Luntz, A. C. Dynamics of Ammonia Decomposition on Ru(0001). *J. Chem. Phys.* **2000**, *113*, 6882–6887, DOI: [10.1063/1.1310662](https://doi.org/10.1063/1.1310662).
- (26) Hu, X.; Yang, M.; Xie, D.; Guo, H. Vibrational Enhancement in the Dynamics of Ammonia Dissociative Chemisorption on Ru(0001). *J. Chem. Phys.* **2018**, *149*, 044703, DOI: [10.1063/1.5043517](https://doi.org/10.1063/1.5043517).
- (27) Jiang, B.; Guo, H. Permutation Invariant Polynomial Neural Network Approach to Fitting Potential Energy Surfaces. III. Molecule-Surface Interactions. *J. Chem. Phys.* **2014**, *141*, 034109, DOI: [10.1063/1.4887363](https://doi.org/10.1063/1.4887363).
- (28) Perdew, J. P.; Burke, K.; Ernzerhof, M. Generalized Gradient Approximation Made Simple. *Phys. Rev. Lett.* **1996**, *77*, 3865–3868, DOI: [10.1103/PhysRevLett.77.3865](https://doi.org/10.1103/PhysRevLett.77.3865).
- (29) Perdew, J. P.; Wang, Y. Accurate and Simple Analytic Representation of the Electron-Gas Correlation Energy. *Phys. Rev. B* **1992**, *45*, 13244–13249, DOI: [10.1103/PhysRevB.45.13244](https://doi.org/10.1103/PhysRevB.45.13244).
- (30) Díaz, C.; Pijper, E.; Olsen, R. A.; Busnengo, H. F.; Auerbach, D. J.; Kroes, G. J. Chemically Accurate Simulation of a Prototypical Surface Reaction: H₂ Dissociation on Cu(111). *Science* **2009**, *326*, 832–834, DOI: [10.1126/science.1178722](https://doi.org/10.1126/science.1178722).
- (31) Wijzenbroek, M.; Kroes, G. J. The Effect of the Exchange-Correlation Functional on H₂ Dissociation on Ru(0001). *J. Chem. Phys.* **2014**, *140*, 084702, DOI: [10.1063/1.4865946](https://doi.org/10.1063/1.4865946).

- (32) Nattino, F.; Ueta, H.; Chadwick, H.; van Reijzen, M. E.; Beck, R. D.; Jackson, B.; van Hemert, M. C.; Kroes, G.-J. Ab Initio Molecular Dynamics Calculations versus Quantum-State-Resolved Experiments on $\text{CHD}_3 + \text{Pt}(111)$: New Insights into a Prototypical Gas–Surface Reaction. *J. Phys. Chem. Lett.* **2014**, *5*, 1294–1299, DOI: [10.1021/jz500233n](https://doi.org/10.1021/jz500233n).
- (33) Nattino, F.; Migliorini, D.; Bonfanti, M.; Kroes, G.-J. Methane Dissociation on Pt(111): Searching for a Specific Reaction Parameter Density Functional. *J. Chem. Phys.* **2016**, *144*, 044702, DOI: [10.1063/1.4939520](https://doi.org/10.1063/1.4939520).
- (34) Hammer, B.; Hansen, L. B.; Nørskov, J. K. Improved Adsorption Energetics within Density-Functional Theory Using Revised Perdew-Burke-Ernzerhof Functionals. *Phys. Rev. B* **1999**, *59*, 7413–7421, DOI: [10.1103/PhysRevB.59.7413](https://doi.org/10.1103/PhysRevB.59.7413).
- (35) Dion, M.; Rydberg, H.; Schröder, E.; Langreth, D. C.; Lundqvist, B. I. Van Der Waals Density Functional for General Geometries. *Phys. Rev. Lett.* **2004**, *92*, 246401, DOI: [10.1103/PhysRevLett.92.246401](https://doi.org/10.1103/PhysRevLett.92.246401).
- (36) Kresse, G.; Hafner, J. Ab Initio Molecular-Dynamics Simulation of the Liquid-Metal–Amorphous-Semiconductor Transition in Germanium. *Phys. Rev. B* **1994**, *49*, 14251–14269, DOI: [10.1103/PhysRevB.49.14251](https://doi.org/10.1103/PhysRevB.49.14251).
- (37) Kresse, G.; Hafner, J. Ab Initio Molecular Dynamics for Liquid Metals. *Phys. Rev. B* **1993**, *47*, 558–561, DOI: [10.1103/PhysRevB.47.558](https://doi.org/10.1103/PhysRevB.47.558).
- (38) Kresse, G.; Furthmüller, J. Efficient Iterative Schemes for Ab Initio Total-Energy Calculations Using a Plane-Wave Basis Set. *Phys. Rev. B* **1996**, *54*, 11169–11186, DOI: [10.1103/PhysRevB.54.11169](https://doi.org/10.1103/PhysRevB.54.11169).
- (39) Kresse, G.; Furthmüller, J. Efficiency of Ab-Initio Total Energy Calculations for Metals and Semiconductors Using a Plane-Wave Basis Set. *Comput. Mater. Sci.* **1996**, *6*, 15–50, DOI: [10.1016/0927-0256\(96\)00008-0](https://doi.org/10.1016/0927-0256(96)00008-0).
- (40) Kresse, G.; Joubert, D. From Ultrasoft Pseudopotentials to the Projector Augmented-Wave Method. *Phys. Rev. B* **1999**, *59*, 1758–1775, DOI: [10.1103/PhysRevB.59.1758](https://doi.org/10.1103/PhysRevB.59.1758).
- (41) Blöchl, P. E. Projector Augmented-Wave Method. *Phys. Rev. B* **1994**, *50*, 17953–17979, DOI: [10.1103/PhysRevB.50.17953](https://doi.org/10.1103/PhysRevB.50.17953).
- (42) Methfessel, M.; Paxton, A. T. High-Precision Sampling for Brillouin-Zone Integration in Metals. *Phys. Rev. B* **1989**, *40*, 3616–3621, DOI: [10.1103/PhysRevB.40.3616](https://doi.org/10.1103/PhysRevB.40.3616).

- (43) Henkelman, G.; Jónsson, H. A Dimer Method for Finding Saddle Points on High Dimensional Potential Surfaces Using Only First Derivatives. *J. Chem. Phys.* **1999**, *111*, 7010–7022, DOI: [10.1063/1.480097](https://doi.org/10.1063/1.480097).
- (44) Heyden, A.; Bell, A. T.; Keil, F. J. Efficient Methods for Finding Transition States in Chemical Reactions: Comparison of Improved Dimer Method and Partitioned Rational Function Optimization Method. *J. Chem. Phys.* **2005**, *123*, 224101, DOI: [10.1063/1.2104507](https://doi.org/10.1063/1.2104507).
- (45) Kästner, J.; Sherwood, P. Superlinearly Converging Dimer Method for Transition State Search. *J. Chem. Phys.* **2008**, *128*, 014106, DOI: [10.1063/1.2815812](https://doi.org/10.1063/1.2815812).
- (46) Xiao, P.; Sheppard, D.; Rogal, J.; Henkelman, G. Solid-State Dimer Method for Calculating Solid-Solid Phase Transitions. *J. Chem. Phys.* **2014**, *140*, 174104, DOI: [10.1063/1.4873437](https://doi.org/10.1063/1.4873437).
- (47) Transition State Tools Package for VASP <https://theory.cm.utexas.edu/vtsttools/index.html> (accessed 02/08/2021).
- (48) Arblaster, J. W. Crystallographic Properties of Ruthenium. *Platin. Met. Rev.* **2013**, *57*, 127–136, DOI: [10.1595/147106713X665030](https://doi.org/10.1595/147106713X665030).
- (49) Mondal, A.; Wijzenbroek, M.; Bonfanti, M.; Díaz, C.; Kroes, G.-J. Thermal Lattice Expansion Effect on Reactive Scattering of H₂ from Cu(111) at T_s = 925 K. *J. Phys. Chem. A* **2013**, *117*, 8770–8781, DOI: [10.1021/jp4042183](https://doi.org/10.1021/jp4042183).
- (50) Migliorini, D.; Chadwick, H.; Nattino, F.; Gutiérrez-González, A.; Dombrowski, E.; High, E. A.; Guo, H.; Utz, A. L.; Jackson, B.; Beck, R. D.; Kroes, G.-J. Surface Reaction Barriometry: Methane Dissociation on Flat and Stepped Transition-Metal Surfaces. *J. Phys. Chem. Lett.* **2017**, *8*, 4177–4182, DOI: [10.1021/acs.jpcllett.7b01905](https://doi.org/10.1021/acs.jpcllett.7b01905).
- (51) Blöchl, P. E.; Jepsen, O.; Andersen, O. K. Improved Tetrahedron Method for Brillouin-Zone Integrations. *Phys. Rev. B* **1994**, *49*, 16223–16233, DOI: [10.1103/PhysRevB.49.16223](https://doi.org/10.1103/PhysRevB.49.16223).
- (52) Mermin, N. D. Thermal Properties of the Inhomogeneous Electron Gas. *Phys. Rev.* **1965**, *137*, A1441–A1443, DOI: [10.1103/PhysRev.137.A1441](https://doi.org/10.1103/PhysRev.137.A1441).
- (53) Benndorf, C.; Madey, T. E. Adsorption and Orientation of NH₃ on Ru(001). *Surf. Sci.* **1983**, *135*, 164–183, DOI: [10.1016/0039-6028\(83\)90217-0](https://doi.org/10.1016/0039-6028(83)90217-0).
- (54) Maier, S.; Stass, I.; Cerda, J. I.; Salmeron, M. Bonding of Ammonia and Its Dehydrogenated Fragments on Ru(0001). *J. Phys. Chem. C* **2012**, *116*, 25395–25400, DOI: [10.1021/jp308835x](https://doi.org/10.1021/jp308835x).

- (55) Luntz, A. C.; Bethune, D. S. Activation of Methane Dissociation on a Pt(111) Surface. *J. Chem. Phys.* **1989**, *90*, 1274–1280, DOI: [10.1063/1.456132](https://doi.org/10.1063/1.456132).
- (56) Tiwari, A. K.; Nave, S.; Jackson, B. The Temperature Dependence of Methane Dissociation on Ni(111) and Pt(111): Mixed Quantum-Classical Studies of the Lattice Response. *J. Chem. Phys.* **2010**, *132*, 134702, DOI: [10.1063/1.3357415](https://doi.org/10.1063/1.3357415).
- (57) King, D. A.; Wells, M. G. Reaction Mechanism in Chemisorption Kinetics: Nitrogen on the {100} Plane of Tungsten. *Proc. R. Soc. Lond. A* **1974**, *339*, 245–269, DOI: [10.1098/rspa.1974.0120](https://doi.org/10.1098/rspa.1974.0120).
- (58) Gerrits, N.; Kroes, G.-J. Curious Mechanism of the Dissociative Chemisorption of Ammonia on Ru(0001). *J. Phys. Chem. C* **2019**, *123*, 28291–28300, DOI: [10.1021/acs.jpcc.9b09121](https://doi.org/10.1021/acs.jpcc.9b09121).
- (59) Jiang, B.; Guo, H. Dynamics of Water Dissociative Chemisorption on Ni(111): Effects of Impact Sites and Incident Angles. *Phys. Rev. Lett.* **2015**, *114*, 166101, DOI: [10.1103/PhysRevLett.114.166101](https://doi.org/10.1103/PhysRevLett.114.166101).
- (60) Zhang, Z.; Liu, T.; Fu, B.; Yang, X.; Zhang, D. H. First-Principles Quantum Dynamical Theory for the Dissociative Chemisorption of H₂O on Rigid Cu(111). *Nat. Commun.* **2016**, *7*, 11953, DOI: [10.1038/ncomms11953](https://doi.org/10.1038/ncomms11953).
- (61) Shen, X.; Zhang, Z.; Zhang, D. H. Communication: Methane Dissociation on Ni(111) Surface: Importance of Azimuth and Surface Impact Site. *J. Chem. Phys.* **2016**, *144*, 101101, DOI: [10.1063/1.4943128](https://doi.org/10.1063/1.4943128).
- (62) Goodman, F. O.; Wachman, H. Y. *Formula for Thermal Accommodation Coefficient*; 66-1; Cambridge, Massachusetts: M.I.T. Fluid Dynamics Research, 1966, DOI: [10.21236/ad0631007](https://doi.org/10.21236/ad0631007).
- (63) Gerrits, N.; Chadwick, H.; Kroes, G.-J. Dynamical Study of the Dissociative Chemisorption of CHD₃ on Pd(111). *J. Phys. Chem. C* **2019**, *123*, 24013–24023, DOI: [10.1021/acs.jpcc.9b05757](https://doi.org/10.1021/acs.jpcc.9b05757).
- (64) Marcus, R. A. On the Analytical Mechanics of Chemical Reactions. Quantum Mechanics of Linear Collisions. *J. Chem. Phys.* **1966**, *45*, 4493–4499, DOI: [10.1063/1.1727528](https://doi.org/10.1063/1.1727528).
- (65) McCullough, E. A.; Wyatt, R. E. Quantum Dynamics of the Collinear (H, H₂) Reaction. *J. Chem. Phys.* **1969**, *51*, 1253–1254, DOI: [10.1063/1.1672133](https://doi.org/10.1063/1.1672133).
- (66) David, C. W. IR Vibration-Rotation Spectra of the Ammonia Molecule. *J. Chem. Educ.* **1996**, *73*, 46, DOI: [10.1021/ed073p46](https://doi.org/10.1021/ed073p46).

- (67) Marquardt, R.; Sagui, K.; Zheng, J.; Thiel, W.; Luckhaus, D.; Yurchenko, S.; Mariotti, F.; Quack, M. Global Analytical Potential Energy Surface for the Electronic Ground State of NH_3 from High Level Ab Initio Calculations. *J. Phys. Chem. A* **2013**, *117*, 7502–7522, DOI: [10.1021/jp4016728](https://doi.org/10.1021/jp4016728).
- (68) Halpern, A. M.; Ramachandran, B. R.; Glendening, E. D. The Inversion Potential of Ammonia: An Intrinsic Reaction Coordinate Calculation for Student Investigation. *J. Chem. Educ.* **2007**, *84*, 1067, DOI: [10.1021/ed084p1067](https://doi.org/10.1021/ed084p1067).
- (69) Bisson, R.; Sacchi, M.; Dang, T. T.; Yoder, B.; Maroni, P.; Beck, R. D. State-Resolved Reactivity of $\text{CH}_4(2\nu_3)$ on Pt(111) and Ni(111): Effects of Barrier Height and Transition State Location. *J. Phys. Chem. A* **2007**, *111*, 12679–12683, DOI: [10.1021/jp076082w](https://doi.org/10.1021/jp076082w).
- (70) Ghassemi, E. N.; Somers, M. F.; Kroes, G.-J. Assessment of Two Problems of Specific Reaction Parameter Density Functional Theory: Sticking and Diffraction of H_2 on Pt(111). *J. Phys. Chem. C* **2019**, *123*, 10406–10418, DOI: [10.1021/acs.jpcc.9b00981](https://doi.org/10.1021/acs.jpcc.9b00981).

